



Integrated moisture transport variability over China: patterns, impacts, and relationship with El Nino–Southern Oscillation (ENSO)

Olusola O. Ayantobo^{1,2} · Jiahua Wei^{1,3} · Beiming Kang³ · Guangqian Wang^{1,3}

Received: 10 September 2020 / Accepted: 11 November 2021 / Published online: 24 November 2021
© The Author(s), under exclusive licence to Springer-Verlag GmbH Austria, part of Springer Nature 2021

Abstracts

The transport of atmospheric moisture presents a crucial role in the global hydrological cycle. In this paper, we performed an empirical orthogonal function (EOF) investigation of integrated moisture transport (IVT) which was observed to be connected with the renowned regional climate phenomenon named El Nino–Southern Oscillation (ENSO) in China. Results explained that in the Eastern and Southern China Sea, and Southeastern China, IVT variances were high, and could change significantly yearly. However, in Northern China, variances were quite low, meaning that monthly IVT was more predictable. The spatial distribution of IVT anomalies was different with the seasons. Summer, in particular, exhibited significantly higher IVT values across the equatorial western Pacific, and there was also a transfer of moisture from the tropical Indian Ocean to the Northwestern and Southeastern China. The primary six modes of the EOFs together explained about 52.3%, which accounted for greater than half of the variation in the IVT anomalies. The main mode was related to ENSO and it explained approximately 16.4% variance in the Southern China Sea and central equatorial Pacific, while the second mode illustrated about 10.8% variance and was strongest in the East China Sea and entire Southeastern China. The cross-wavelet coherence indicated that the IVT and ENSO time-series were coherent, having a duration of about 2–8 years. This thus implied that increased IVT was linked with enhanced ENSO activities. This study could contribute to a better perception of how atmospheric circulation patterns could modify the general flow of the atmosphere to affect normal weather conditions in China.

1 Introduction

Moisture transport is the most active process in the atmospheric water cycle and performs a significant function in the global climatic environment (Ma et al., 2018; Guan et al., 2019). The vertical moisture transport affects convective processes and its horizontal transport changes regional water vapor conditions (Peixoto, 1973; Guan et al., 2019). According to Ma et al. (2018), four methodologies have

been employed to describe atmospheric moisture transport attributes: vertically integrated water vapor transport (IVT) (Zhu and Newell, 1998), integrated water vapor distributions (Gimeno et al., 2014), tropical moisture exports using the lagrangian approach, and stable oxygen isotope investigation. Many IVT characteristics, including wind speed, water vapor content, and moisture flux patterns, among others, have been shown to affect the distributions of hydrological extreme events (Gimeno et al., 2014; Ma et al., 2018).

Extreme precipitation events have shown an increasing trend in the last few decades (Fu et al., 2016; Li et al., 2020), and many studies have proven that abundant moisture in the atmospheric column (Li et al., 2020; Yuan et al., 2021) and atmospheric IVT with regard to different atmospheric systems causes precipitation extremes (Lamjiri et al., 2017; Yuan et al., 2021). Moreover, IVT has been shown to be more significant than evapotranspiration in precipitation variability (Ruizbaradas and Nigam, 2013; Yuan et al., 2021). El Nino and Southern Oscillation (ENSO) is a strong climate phenomenon associated with SST anomalies in the tropical Pacific Ocean and is one of the most widely discussed atmospheric systems (McPhaden et al., 2006; Sun

✉ Jiahua Wei
weijiahua@tsinghua.edu.cn

¹ Department of Hydraulic Engineering, State Key Laboratory of Hydroscience and Engineering, Tsinghua University, Beijing, China

² Department of Water Resources Management and Agricultural-Meteorology, Federal University of Agriculture, Abeokuta, Nigeria

³ State Key Laboratory of Plateau Ecology and Agriculture, School of Water Resources and Electric Engineering, Laboratory of Ecological Protection and High Quality Development in the Upper Yellow River, Qinghai University, Xining 810016, China

and Yang 2012). Their development provides a strong signal of interannual climate variability (Sun and Yang 2012; Yu et al., 2019).

ENSO events can have a significant impact on temperature, circulation, and precipitation through the Pacific-East Asian teleconnection (Li et al., 2016; Yu et al., 2019). It could influence the strength and position of the Western Pacific Subtropical High (WPSH) in the East Asian microclimate (Zhang, 2020), resulting in anticyclonic anomalies that are capable of generating precipitation variability across southern China (Chen et al., 2014; Kao and Yu 2009; Wang et al. 2000; Kim et al., 2017; Yu et al., 2019). Thus, when the WPSH is strong and intrudes into the west, more moisture is transported from the east to southern China, and when the WPSH retreats to the east, less moisture is contributed from the east (Chen et al., 2014; Ayantobo et al., 2019; Zhang, 2020).

Studies have revealed that precipitation across the southern parts of northeastern China as well as within the Yellow River basin has greatly decreased in the past few decades (Li et al., 2012; Qian and Qin 2008), and it has been asserted that Northern China apparently commenced a dry-spell following the year 1977 (Zhou and Huang 2003; Li et al., 2012). Contrarily, enhanced precipitation was observed across Southeastern China and the Yangtze-Huaihe River basin in the late 1970s, shifting from a dry to a wet season and resulting in repeated floods and great socioeconomic damage (Gong and Ho 2002). Furthermore, severe drought events which persisted in South China from the beginning of winter to the end of spring in 2011 destroyed more than 98.9 million hectares while more than 4.9 and 3.4 million people and livestock, respectively, had inadequate potable water (Sun and Yang 2012; Chen et al., 2014; Ayantobo et al., 2019).

This obvious interdecadal variability in summer precipitation across Eastern China is not just a regional event but includes the outcome of notable fluctuations in the weather mechanism across Eastern Asia (Li et al., 2012). The physical mechanisms describing moisture transport roles and related synoptic-scale flow patterns are complicated (Feng and Zhou, 2012; Ma et al., 2018) and require further diagnostic analysis especially in the climatic regions of China, which have not been previously studied. We attempted to investigate the predominant modes of IVT by employing empirical orthogonal function (EOF). The EOF separates moisture transport anomalies signal into sum of orthogonal modes through optimizing the variances demonstrated by individual mode (Messie and Chavez 2011).

Though drought and flood event causes have been considered, linkages with IVT have recently begun to be investigated (Herrera-Estrada et al., 2019; Roy et al. 2019). Inspired by these linkages, it is imperative to understand IVT's role in the propagation of floods and droughts. Although reports on

ENSO have improved, their mechanisms, forcing, and long-term evolution as they relate to IVT are still poorly understood (Messie and Chavez 2011). Hence, we used wavelet analysis to explore how ENSO could autonomously affect IVT. Overall, this study aims to understand IVT variability, explore its role in propagation of floods and droughts, and understand its relationship with ENSO across climatic regions of China between 1980 and 2016. Following this introduction, Sect. 2 explains the datasets and all analytical approaches. Section 3 presents the results and discussions, while the summary and conclusions are presented in Sect. 5.

2 Study area, datasets, and methods

2.1 Study area

China is located between 14°–58°N and 75°–135°E with a large geographic size, enriched with several landforms that comprise deserts, high-elevation mountains, and hills in the western regions, while in the central and eastern regions, the landmass slopes into deltas and extensive plains. In order to study the regional relationship between IVT and ENSO, China was divided into seven climatic regions as shown in Fig. 1. Regions 1 to 7, with varying watershed size, represent the Northeastern humid/semi-humid warm zone, Northern China humid/semi-humid temperate region, Central and South China humid sub-tropical area, Southern China humid tropical area, Inner Mongolia steppe area, Northwestern desert area, and Qinghai-Tibet Plateau, respectively, while the entire mainland China is represented as EMC (Zhao, 1983; Wu et al., 2011; Ayantobo et al., 2017). The east coast of China is affected by the eastern Asian summer monsoon. The Southwest China (SWC) is controlled by a mixture of eastern Asia and Indian summer monsoons, while the northwest regions remain unchanged by the monsoons. Because the most prominent parts of China are located within the Eastern Asia monsoon climate boundary, the variations in precipitation and other climatic variables are obvious (Ayantobo et al., 2017; Wu et al., 2011).

2.2 Datasets

The Climate Forecast System Reanalysis (CFSR) provided by the National Centers for Environmental Prediction (NCEP) used in this study combines significant improvements, such as the higher resolution of T382 (~38 km), having 64 pressure altitudes from the surface down to 0.26 hPa. According to Saha et al. (2010), CFSR employs NCEP coupled forecast models comprised of spectral aerial and modular sea models and employs three-dimensional variable dataset assimilation in accordance with the grid by grid analytical interpolation plot. The CFSR

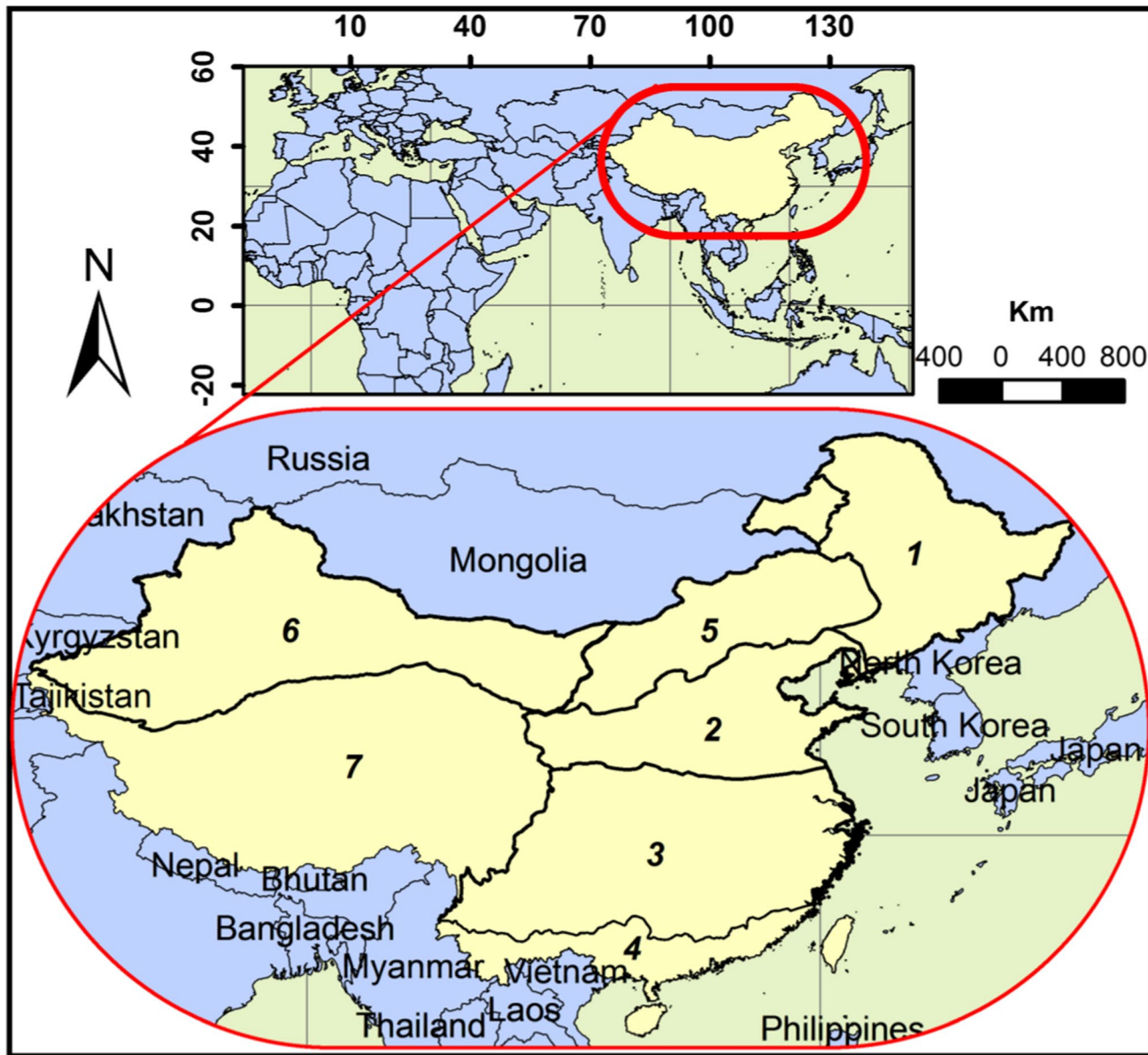


Fig. 1 Geographical map showing seven climatic regions in mainland China and neighboring countries

datasets are accessible on a 6-hourly basis between 1979 and 2010, while CFSv2, the continuation of the CFSR, is obtainable from 2011 forward from NCAR's Research Data Record (<https://rda.ucar.edu>). The investigation time period of 1980–2016 has been selected and the variables chosen for analysis are each day precipitation (mm/day) and specific humidity (kg/kg) at 8 isobaric surfaces (1000, 925, 850, 700, 600, 500, 400, and 300 hPa). Since these datasets are provided four times daily, every day's mean is computed by averaging the sub-day values. Furthermore, we use the National Oceanic and Atmospheric Administration (NOAA) Extended Reconstruction mean monthly

sea surface temperature, sea level pressure, meridional and zonal wind, atmospheric temperature, and cloudiness fraction (Smith et al., 2008), which are accessible at 2.5° grids covering 1854 to date (<http://www.esrl.noaa.gov/psd/data/gridded/>) to derive Nino-3 (50S–50 N, 900–1500 W), Nino-3.4 (50S–50 N, 1700–1200 W), Nino-4 (50S–50 N, 1600E–1500 W), and MEI.v2 indices. These indices are selected to characterize ENSO phases and are used to reveal relationships with IVT since they can represent the average equatorial sea surface temperature anomalies and have been adopted in previous studies (Hao et al., 2019; Huang et al., 2019).

2.3 Methods

2.3.1 Quantification of moisture transport

The distribution and movement of atmospheric moisture transport in this study are quantified using IVT, which is from the water vapor mixing ratios, including zonal winds (u ; m/s), meridional winds (v ; m/s), and specific humidity (q ; kg/kg) from 1000 hPa up to 300 hPa (Ma et al., 2018). The resulting components on individual grid points are then added vertically starting from the surface until about 300 hPa, and later consolidated into horizontal moisture transport vector, having kg/m/s units (Zhu and Newell, 1998; Ma et al., 2018).

$$\text{IVT} = \sqrt{\left(\frac{1}{g} \int_{300}^{1000} qudp \right)^2 + \left(\frac{1}{g} \int_{300}^{1000} qvdp \right)^2} \quad (1)$$

A comprehensive review of this procedure can be read in Zhu and Newell (1998).

2.3.2 Flood and Drought events identification

The Standardized Precipitation Index (SPI) used is based on an equiprobability change of accumulated monthly precipitation into a standard ordinary variable (McKee et al., 1995). SPI is estimated through fitting an incomplete gamma probability density function (PDF) on aggregated monthly precipitation series. The PDF is integrated to get the cumulative probability distribution function $G(x)$, represented as Ayantobo et al., (2017):

$$G(x) = \int_0^x g(x)dx = \frac{1}{\beta^\gamma \Gamma(\gamma)} \int_0^x t^{\gamma-1} e^{-x/\beta} dt \quad (2)$$

where x , β , γ , and Γ represent P amount, shape parameter, scale parameter, and gamma function, respectively. Making $t = x/\beta$ produces the incomplete gamma function:

$$G(x) = \frac{1}{\Gamma(\gamma)} \int_0^x t^{\gamma-1} e^{-t} dt \quad (3)$$

Knowing that the gamma function is undefined for $x=0$ and the precipitation distribution might include zeros, the cumulative probability then becomes:

$$H(x) = q + (1 - q)G(x) \quad (4)$$

Here, q represents the possibility of zero precipitation. $H(x)$ is later converted into standard normal SPI using Abramowitz and Stegun (1965) approximation. The SPI

are symmetrical and could be employed for recognizing flood and drought scenarios (Ayantobo et al., 2017).

Moreover, the IVT, precipitation, SPI, and SST datasets are normalized to take the values to a standard scale of 0–1. So, the normalization is achieved by adopting the expression below:

$$X_{\text{norm}} = \frac{(X - X_{\min})}{(X_{\max} - X_{\min})} \quad (5)$$

where X_{norm} represents the normalized value, X is the time series of input data, X_{\max} represents highest number within the dataset, and X_{\min} is the smallest number in the series.

2.3.3 Empirical orthogonal function analysis

Following the elimination of local linear trends and seasonal cycles from the monthly IVT, the EOF analysis is then employed to investigate the spatiotemporal pattern of the moisture transport across the climatic regions of China from 1980 to 2016. This approach has been popularly applied regionally within the ocean basin, and lots of indices are estimated employing EOFs. EOFs can separate the moisture transport anomaly signal into orthogonal modes through optimizing the variance described via individual mode (Messie and Chavez 2011). Every mode will comprise of a spatial pattern (i.e., the EOF) and a principal component (i.e., PC) statistic which depicts the temporal distribution of the EOF pattern. Interestingly, a particular mode may be reproduced through multiplying the spatial EOF by its corresponding PC in time (Messie and Chavez 2011).

2.3.4 Wavelet analysis

To examine the coherence and frequency between IVT and ENSO, we performed wavelet analyses in different climatic regions. Wavelet analyses have been extensively utilized in oceanography, especially, to examine ENSO (Kao and Yu 2009; Messie and Chavez 2011). Here, the signal is decomposed into time and frequency in space to focus on the predominant variability scales and its respective periods. This process is termed time-variation Fourier analyses, demonstrating energy not solely as a function of frequency but likewise of time period (Messie and Chavez 2011; Torrence and Compo 1998). The continuous wavelength transform (CWT) of a consecutive, square-integrable function $x(t)$ at a scale $a > 0$ and translational value $b \in R$ is represented using the integral below:

$$W_x(a, b) = \frac{1}{\sqrt{|a|}} \int_{-\infty}^{+\infty} x(t) \psi^* S\left(\frac{t-b}{a}\right) dt \quad (6)$$

Here, $\psi(t)$ represents the continuous function in both time and frequency domain modes termed the mother wavelet and $*$ indicates complex conjugate operation. Studies have shown that mother wavelet may give a root functions to produce the daughter wavelets that are just the transposed and scaled variants of the initial mother wavelet. More reports about the methods and applicability of CWT have been documented (Grinsted et al., 2004; Torrence and Compo, 1998).

3 Results and discussion

3.1 Patterns of moisture transport variability

Moisture transport is the most active process in the atmospheric water cycle because the vertical transport could affect convective processes while its horizontal transport could change regional water vapor conditions, thereby affecting precipitation in downstream regions (Peixoto, 1973; Guan et al., 2019). Therefore, in this section, we examined the spatial variability of interannual and seasonal IVT to understand their patterns as well as investigate their importance to regional atmospheric water budgets over China.

3.1.1 Interannual variability of moisture transport

The main question was, how predictable are monthly IVT values? For instance, will the moisture transport in January next year be about the same as it was in January of last year, or will there be a tremendous amount of variability between Januaries? What could be the cause of the interannual variability? To address this question, we thoroughly examined the mean monthly IVT as well as its corresponding variance between 1980 and 2016 and produced the monthly spatial maps in Fig. 2. In general, high mean and variance values were observed across the ocean in June, July, August, and September, which, according to previous studies, might be connected to a greater evaporation rate from water bodies (Ghodichore et al. 2017). Our results showed that the observed IVT values over the Bay of Bengal, Southern, and the Eastern China Sea are very high and will vary significantly. The Bay of Bengal was marked by a Southwestern IVT anomaly, which conveys moisture to the northeastern regions near 30°N and links with the mid-latitude Westerly IVT anomalies, while the Southern China Sea was marked by a southerly IVT anomaly, making these regions significant moisture sources (Maussion et al., 2014; Zhang, 2020). We observed high variances in the southeastern region, indicating that monthly IVT could change significantly from year to year, but during the same period in the northern region, the mean IVT was low and the variance was fairly low, indicating that monthly IVT is more predictable from climatology. The interannual variability of IVT can

be utilized to give evidence and more profound insight into hydrological extreme situations such as floods and droughts (Li and Lin 2018; Zhang, 2020).

3.1.2 Seasonal variability of moisture transport

Figure 3 shows the seasonal mean IVT spatial distribution and its corresponding flux divergence. The IVT distribution was found to be different from season to season. Summer, in particular, exhibited significantly higher IVT values when compared with other seasons, particularly across the ocean. The IVT anomalies in the Equatorial Western Pacific are obvious and widespread, and there was also a moisture conveyor from the Tropical Indian Ocean to the Northwestern and Southeastern regions of China. The diverging winds sweep from Southern China to the Equatorial Western Pacific and later meet with the winds from the Equatorial Central Pacific. Over mainland China, high IVT values are noticed in summer and followed by spring in the Southeast and a comparatively smaller quantity across the Tibet Plateau.

The climatology of moisture transport during summer across Eastern China has been frequently examined in earlier research (Simmonds et al., 1999). An enormous expanse stretching from the Tropical Indian Ocean and Southern Asia towards Eastern Asia and the Western North Pacific is affected by the Southeasterly and Southwesterly monsoon winds, which serve as a moisture sink in summer. The dominant moisture source contributing to the Tibet Plateau was a nearly tropical-subtropical area of the Indian landmass towards the Southern Hemisphere. Besides, two other moisture origins were identified within the Northwest region of the Tibetan Plateau and also the Bay of Bengal (Ma et al., 2018; Chen et al., 2012). Moisture from the Bay of Bengal travels through the Brahmaputra groove and influences precipitation characteristics in the South-eastern Tibet Plateau (Maussion et al., 2014), whereas moisture from the Northern Indian landmass has a large impact on SWC (Dong et al., 2016).

3.2 Impacts of moisture transport variability on extreme events

The occurrence of extreme events has suggested the need to develop pointers to adequately predict likely severe events to avert major socio-economic disasters. Although many studies have associated the occurrence of extreme events with IVT across many regions across the globe (Lélé et al. 2015; Marengo et al. 2016), such investigations are limited, especially in the SWC where extreme events occur frequently and have caused severe damage in recent decades. The SWC is influenced by the Indian monsoon, the East Asian summer monsoon, and the westerlies, in

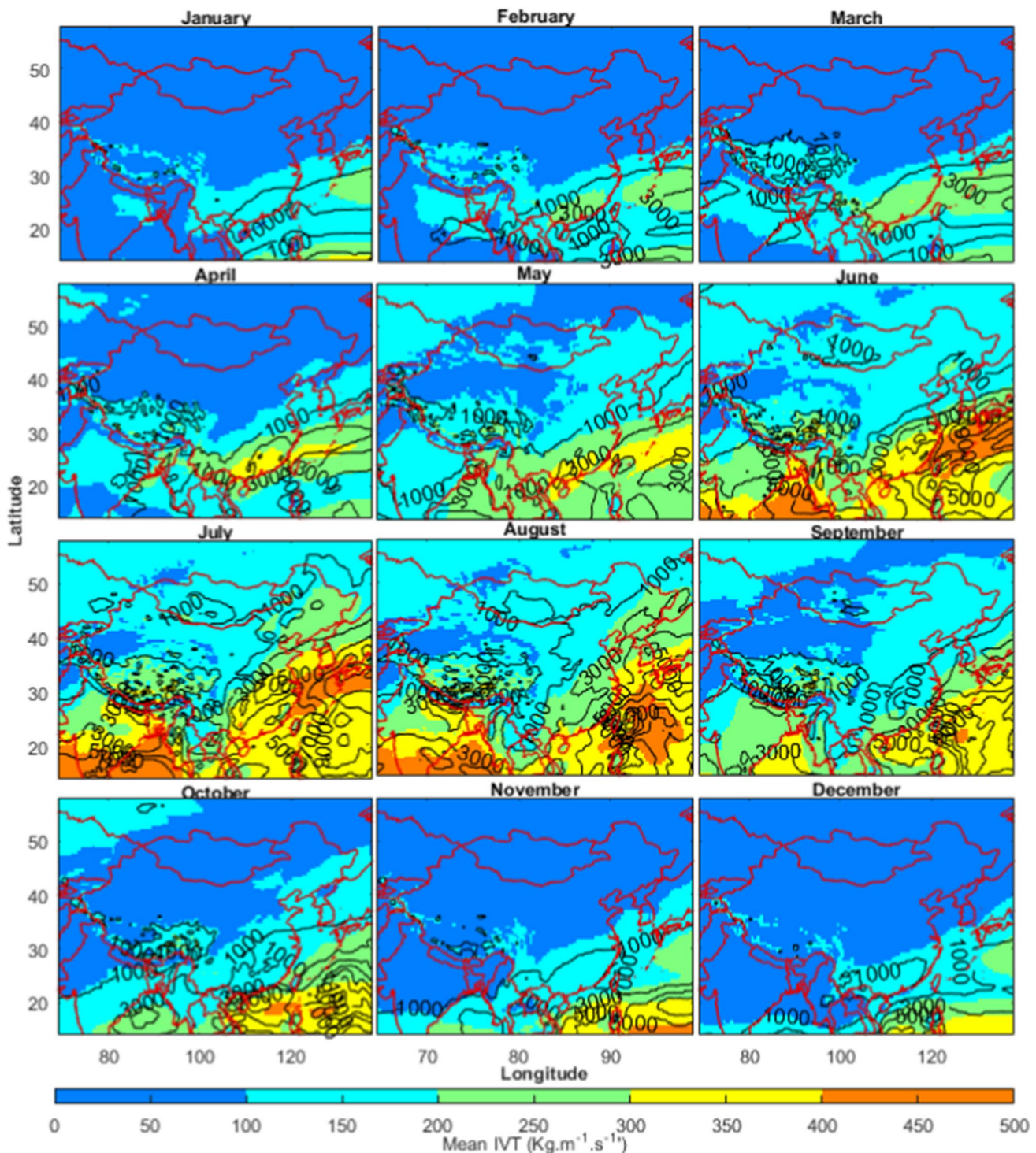


Fig. 2 Spatial distribution of the interannual variation of mean monthly IVT ($\text{kg}/\text{m}/\text{s}$) and variance (kg/m^2) (i.e., contoured) using CFRS reanalyses datasets during 1980–2016 over China and surrounding regions. Contour interval is 1000

which the southwesterly, mid-latitude westerly, southerly, and northerly IVT anomalies produce unusual moisture confluence in southern China. These IVT are significant and play a pivotal role in the spatial propagation of floods

and droughts (Li and Lin 2018; Zhang, 2020). Therefore, in this section, we selected typical flood and drought events in SWC to illustrate IVT impacts on extreme events.

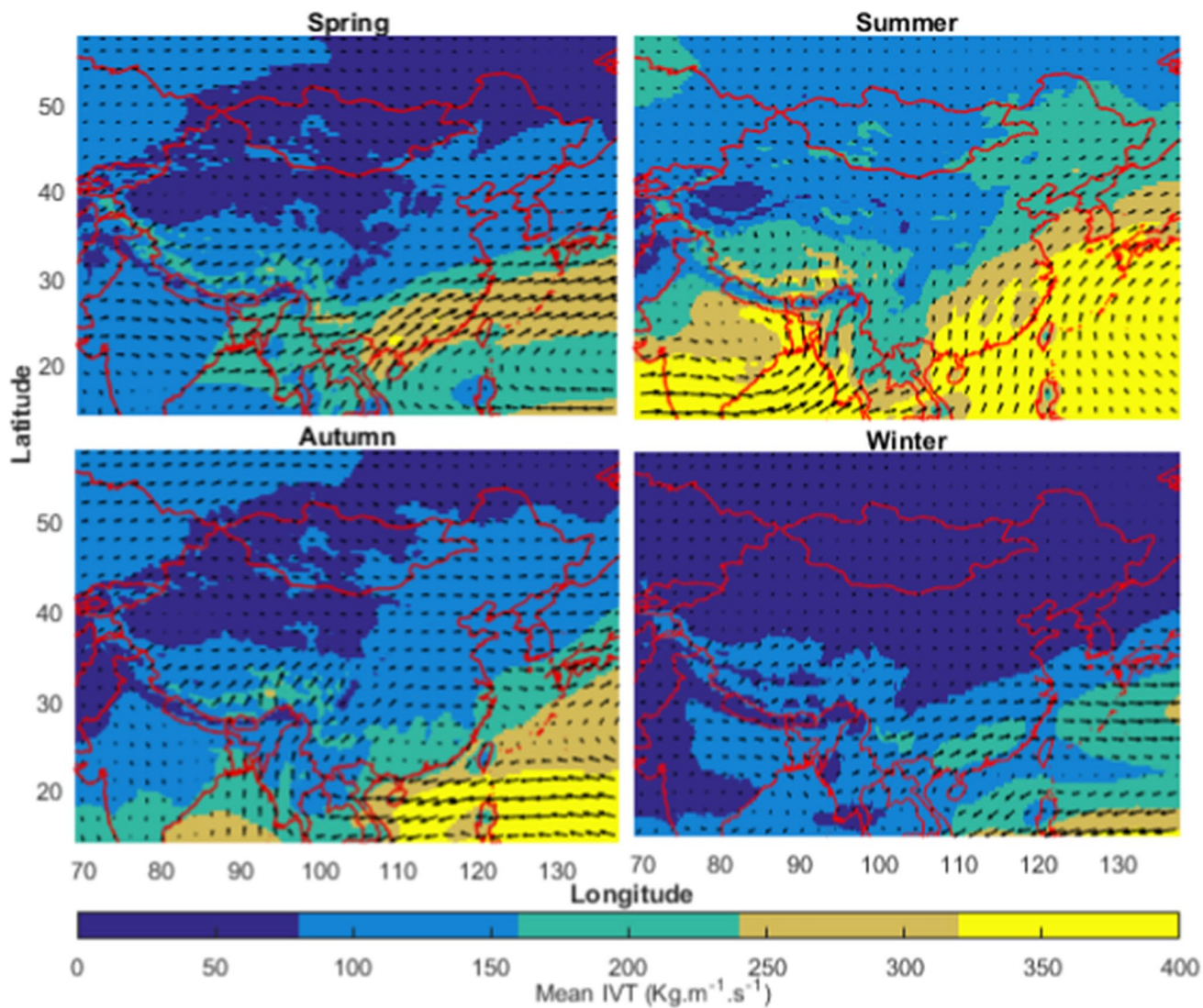


Fig. 3 Seasonal mean distribution of spring, summer, autumn, and winter IVT ($\text{kg}/\text{m}/\text{s}$) and flux divergence using CFRS reanalyses datasets during 1980–2016 over China and surrounding regions

3.2.1 Increased moisture transport intensify flood events

Extreme precipitation events have shown an increasing trend in the last few decades (Fu et al., 2016; Li et al., 2020). Although many factors affect its formation, continuous IVT that changes the local moisture amounts and budget is primary (Yuan et al., 2021). The map in Fig. 4b showed huge IVT of over 400 $\text{kg}/\text{m}/\text{s}$ across southern China, which resulted in a large-scale flood that flooded a greater portion of eastern China in June 1998 (Fig. 4a). During this period, an enhanced IVT to South China from the Southern China Sea joined the Southwesterly IVT from the Northern Bay of Bengal (Li and Lin, 2018), and

resulted in an improved water vapor concentration, consequently increasing the above-average moisture across the region. Moreover, moisture pathways from the tropical Indian Ocean, Yellow Sea, and South China Sea, identified previously during persistent heavy rainfall events, may also have contributed to the flood events (Liu et al., 2016; Yuan et al., 2021). Other studies around the world have proven that IVT with regard to different atmospheric systems are responsible for increased precipitation extremes (Lamjiri et al., 2017; Yuan et al., 2021), while have shown that IVT plays a more important role than evapotranspiration in precipitation variability over the Southern Great Plains (Ruizbaradas and Nigam, 2013; Yuan et al., 2021).

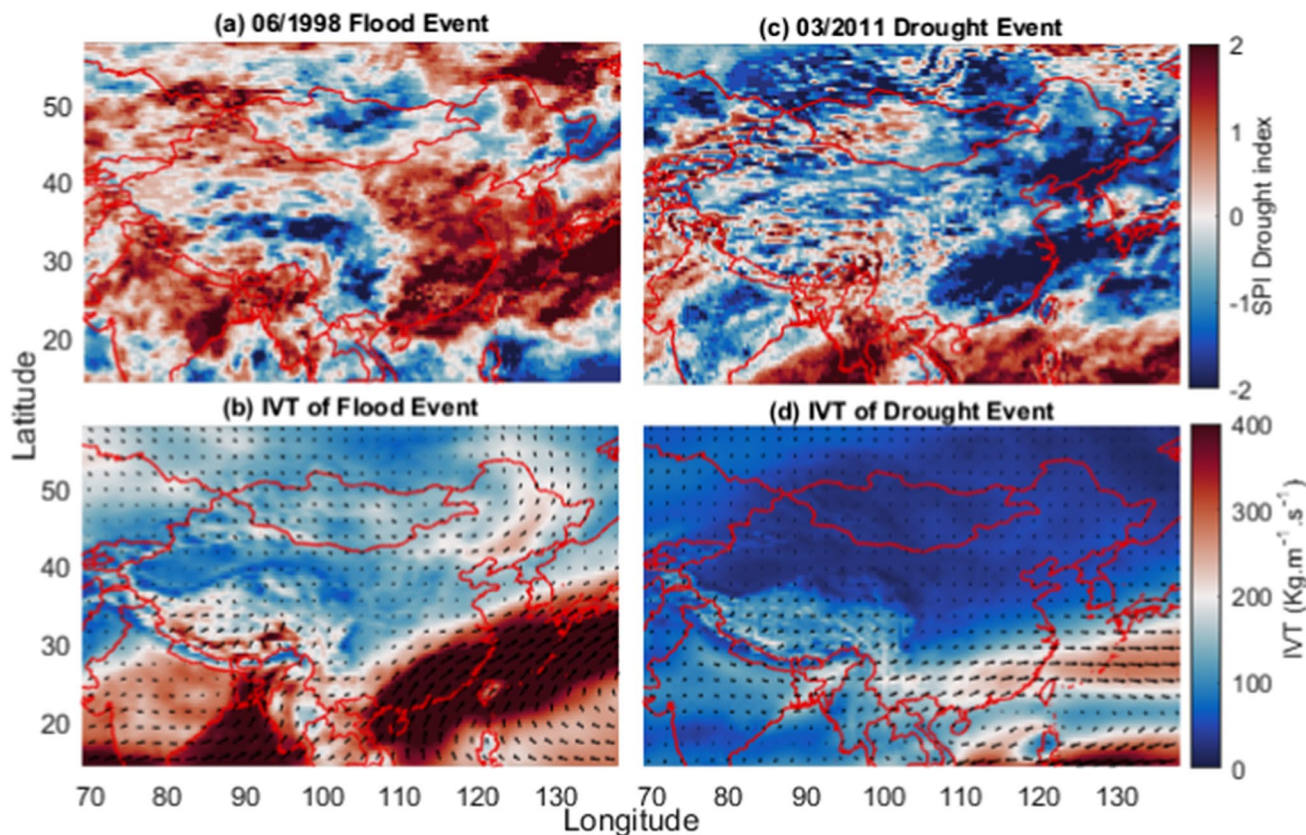


Fig. 4 Spatial pattern of a typical **a** flood event of June 1998 and **c** drought event of March 2011 defined by SPI index and their associated IVTs (kg/m/s) in **b** and **d**, respectively, to illustrate the impacts of moisture transport variations in the spatial propagation of extreme events

3.2.2 Decreased moisture transport amplify drought events

Studies have shown that two large-scale droughts impacted SWC in the summers of 2006 and 2011 and have since been studied especially regarding their meteorological conditions, but not in the context of IVT (Wang et al., 2016; Liu et al., 2017; Zhang, 2020). Figure 4c shows the super drought that occurred during March 2011 and its associated IVT, which was below 250 kg/m/s in most southern regions (Fig. 4d). During this period, the prevailing northeasterly fluxes prohibit southwesterly moisture fluxes to the extent that the circulation change hindered the IVT from the Indian monsoon and the westerlies over SWC, thus causing salient reductions in moisture contributed from the Southwest and West. The circulation anomaly changed consistently, with anomalous moisture fluxes coming from the east, but the small increase could not compensate for the massive decreases from the southwest and west, resulting in an overall significant loss of moisture, amplifying drought (Zhang, 2020). The below-normal moisture that led to the 2011 drought was possibly a combined result of decreased IVT from the North

Indian Ocean and Bay of Bengal, a positive geopotential height anomaly, and a more easterly location of the WPSH, indicating the nonlinearity and complexity in drought formation (Li et al., 2014; Wang et al., 2015; Zhang, 2020). Other studies linking moisture sources to droughts and floods in other regions of the world have shown that droughts in upwind regions can amplify droughts (floods) downwind via decreased (increased) moisture export (Roy et al., 2019; Herrera-Estrada et al., 2019).

3.3 EOF analysis of moisture transport variability

EOF analysis enables us to know not solely where IVT vary, but how often, and what areas tend to vary along or out of phase with one another. In this section, we first considered mean IVT climatology and then examined their spatial trend. Since the absolute variance remaining after detrending and deseasoned the IVT provided limited information on spatial variability, the EOF analysis was also presented and investigated how the modes influences precipitation, drought, and SST anomalies.

3.3.1 Climatological mean, trend, and variance of IVT

Figure 5a shows the spatial pattern of mean IVT climatology across China from 1980 to 2016. We observed massive IVT of nearly 400 kg/m/s across the Bay of Bengal, South, and East China Seas, as well as the coastal areas, which could be linked to high evaporation rates from water masses (Ghodichore et al. 2017). The northern IVT, which ranged between 50 and 100 kg/m/s, was comparatively lower because of the dry air and shorter atmospheric column at the high elevations, which were often affected by the perennial cold Siberian high (Xie et al., 2014; Guan et al., 2019). Moisture transport to the arid region is controlled primarily by three transport belts, including the Westerly Belt, which is the main water vapor source; the Northwesterly Belt, which supplies water vapor from West Siberia; and the Southwesterly Belt that transports water vapor from the Bay of Bengal across Indochina to the east of the Yarlung Zangbo River and the Northern Sichuan Basin (Guan et al., 2019).

Figure 5b shows the spatial trend, which gives an insight into the global warming influence on IVT distribution from 1980 to 2016. The global warming trend was fascinating as the highest positive trend (~ 15 kg/m/s/decade) was seen across the adjoining ocean, while negative trends (~ -10 kg/m/s/decade) dominated most southern parts. The positive trend could result from constant evaporation from water bodies throughout the year compared to landmasses (Ghodichore et al. 2017). Next, knowing that EOF analysis is all about variability and not long-term trends or seasonal variability, we removed IVT trends and also seasonal cycles, which eventually removed the overall mean. The remaining variance in the IVT anomaly after detrending and deseasoning is shown in Fig. 5c, which shows that wherever IVT is large, variance will also be large. The IVT variations showed that the most variable regions transport high moisture. According to Zhang (2020), these variances can serve as an indicator that measures the stability of a contribution from a source.

3.3.2 Modes and principal components of moisture transport

Next, with IVT detrended, mean and seasonal cycle removed, the EOFs are then estimated. All 404 modes in the IVT anomaly were solved and collectively, they explained 100% of the total variance in the IVT anomalies. This implied that at any time, the 404 modes could be summed up, multiplied with their PCs, and still fully reconstruct the time-series without loss of information. For this dataset with natural variability modes, the first few modes carry the most essential information and the residual modes are ignored. Considering the explained variance as a function of the mode number, or as cumulative explained variance, we observed that the first six modes accounted for more than

half of the variation in IVT anomaly, and the rest just added tiny incremental improvements.

The left panel of Fig. 6 depicts the EOF spatial patterns of the first six independent modes, while the right panel shows its associated PCs estimated from 1980 to 2016. This showed that EOFs are not just about time-series, they also give information regarding spatial patterns of variability through time, and each mode obtained has a distinctive pattern of variability, which could assist in explaining why the variance explained by one mode was high compared to other modes. From the spatial patterns, the EOF modes combined explained roughly about 52.3% variance in the IVT anomalies in which the first mode (i.e., 16.4%) described larger than twice more variation than the other modes. Extremely variable regions controlled the analysis and it might be ascertained that the greater part of the variance was in the southern China sea and central equatorial Pacific, while lower IVT variance was observed over southern China. This agrees with previous studies on moisture transport variability (Philander 1986; Messie and Chavez 2011). The associated PC1 from the first mode was dominated by interannual variability, which could possibly be a result of ENSO activities (Kim et al., 2017; Yu et al., 2019).

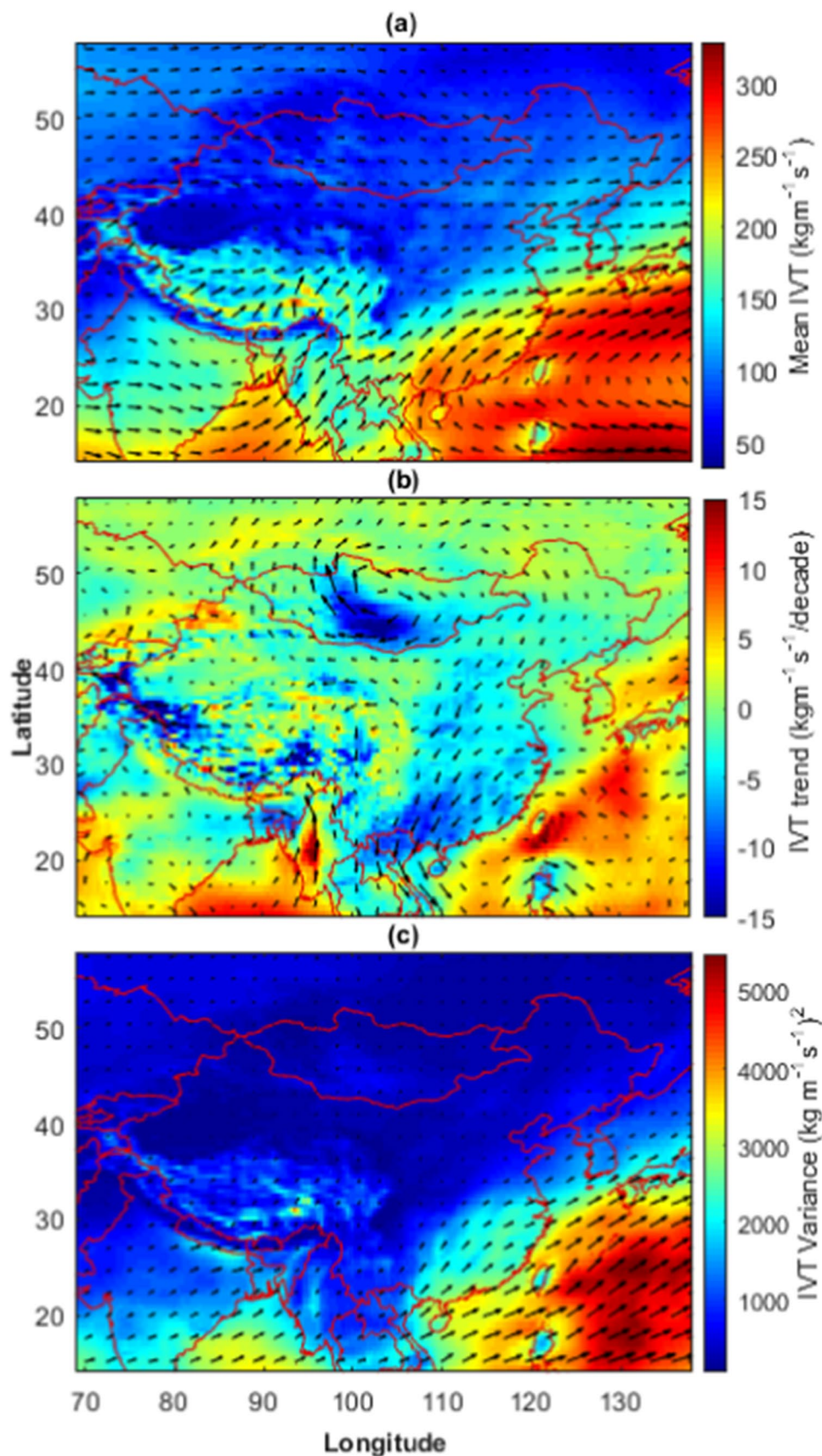
The second mode (i.e., 10.8%) was strongest in the East China Sea and spread towards the entire southeastern China, then decreased gradually towards northwest China. Contrary to the first mode, regions surrounding the South China Sea had much lower IVT variability. Subsequently, the third mode (i.e., 7.9%) had immense variability within the East China Sea, which gradually spread to the southeast and southwest China. Regions around the Bay of Bengal, the Southern China Sea, and the Yellow River had lower variability. The fourth and fifth modes, which had 6.8% and 6.0% IVT anomaly variability, respectively, had higher values in the South China Sea and lower values in the East China Sea.

3.3.3 Relationship between IVT and climatic factors

The spatial pattern of the correlation between PC1 associated with EOF1 and the long-term IVT spatial mean (figure not shown) was similar to the first mode of EOF in Fig. 6, showing that PC1 can adequately represent the variance. High correlations between PC1 and mean IVT ($r^2 \sim 0.8$), significant at a 5% level, dominate the ocean around the South China Sea and Eastern Equatorial Pacific, while a negative correlation was prevalent inland China, with the lowest correlation of $r^2 = -0.5$ around Southern China.

Figure 7 shows the sliding correlation plots of PC1-IVT, PC1-precipitation, PC1-SPI, and PC1-SST with a window of 12-month to understand the connection between the first mode and IVT, precipitation and SST. Generally, the sliding correlation shows obvious interannual changes and ranged from -0.8 to 0.8 . All correlation before 1987

Fig. 5 Spatial distribution of **a** mean monthly IVT ($\text{kg}/\text{m/s}$), **b** IVT trend ($\text{kg}/\text{m/s}/\text{decade}$), and **c** IVT variance ($\text{kg}/\text{m/s}^2$) using CFRS reanalyses datasets during 1980–2016 over mainland China and surrounding regions



was significantly positive except for PC1-precipitation, and an obvious drop in the correlation was seen between 1987–1989, 1992–1994, 1998–1999, and 2007–2009. The negative correlations recovered and became positive after 2010. It was interesting to note that strong negative correlations coincide with some El Niño events. Generally, the correlations for PC1-IVT, PC1-precipitation, and PC1-SST fell below PC1-SPI, meaning that PC1-SPI had a better correlation.

Figure 8 reveals the density scatter plot for the standardized values of PC1 and long-term mean IVT, precipitation, SPI, and SST alongside their root mean square error (RMSE). The RMSE values shown within the scatter plots indicate the general skill of each respective variable. Among all the variables, precipitation displayed the highest RMSE of 0.32, while SPI exhibited the lowest value of 0.23. This proved that drought appeared to be related more to IVT than precipitation and SST. Generally, all variables exhibited weaker correlation, which might be ascribed to the delay factor between moisture buildup and the eventual precipitation (Ghodichore et al. 2017; Dufour et al., 2016).

3.4 Relationship between moisture transport and ENSO

The formation and progression of the Westerly North Pacific anticyclone are linked not only to global SST anomalies in the Equatorial Central-eastern Pacific, but also to local SST anomalies in the Western North Pacific (Wang et al., 2000; Wu and Wang 2000). Hence, in this section, we first focused on the temporal variability of IVT in different climatic regions of China as defined in Fig. 1 and the Nino-3, Nino-3.4, Nino-4, and MEI.v2 indices. These indices were selected to characterize ENSO phases because they can represent average equatorial SST anomalies and have been generally adopted to represent ENSO stages (Hao et al., 2019; Huang et al., 2019). Finally, we examined their relationship using wavelet analysis to show how ENSO could autonomously affect IVT in various climatic regions.

3.4.1 Temporal variability of moisture transport and ENSO

Figure 9a shows the temporal variability of IVT in different regions of China from 1980 to 2016. We observed that IVT over Region 4 was the highest, followed by Region 3. These two regions are located in southern China, which is often influenced by the Indian monsoon, the East Asian summer monsoon, and the westerlies. Moreover, the southwesterly, mid-latitude westerly, southerly, and northerly IVT anomalies produce an unusual moisture confluence in southern China (Li and Lin 2018; Zhang, 2020). Also, the lowest IVT was observed in Region 6 followed by Region 5, representing the Tibetan plateau and the inner Mongolia

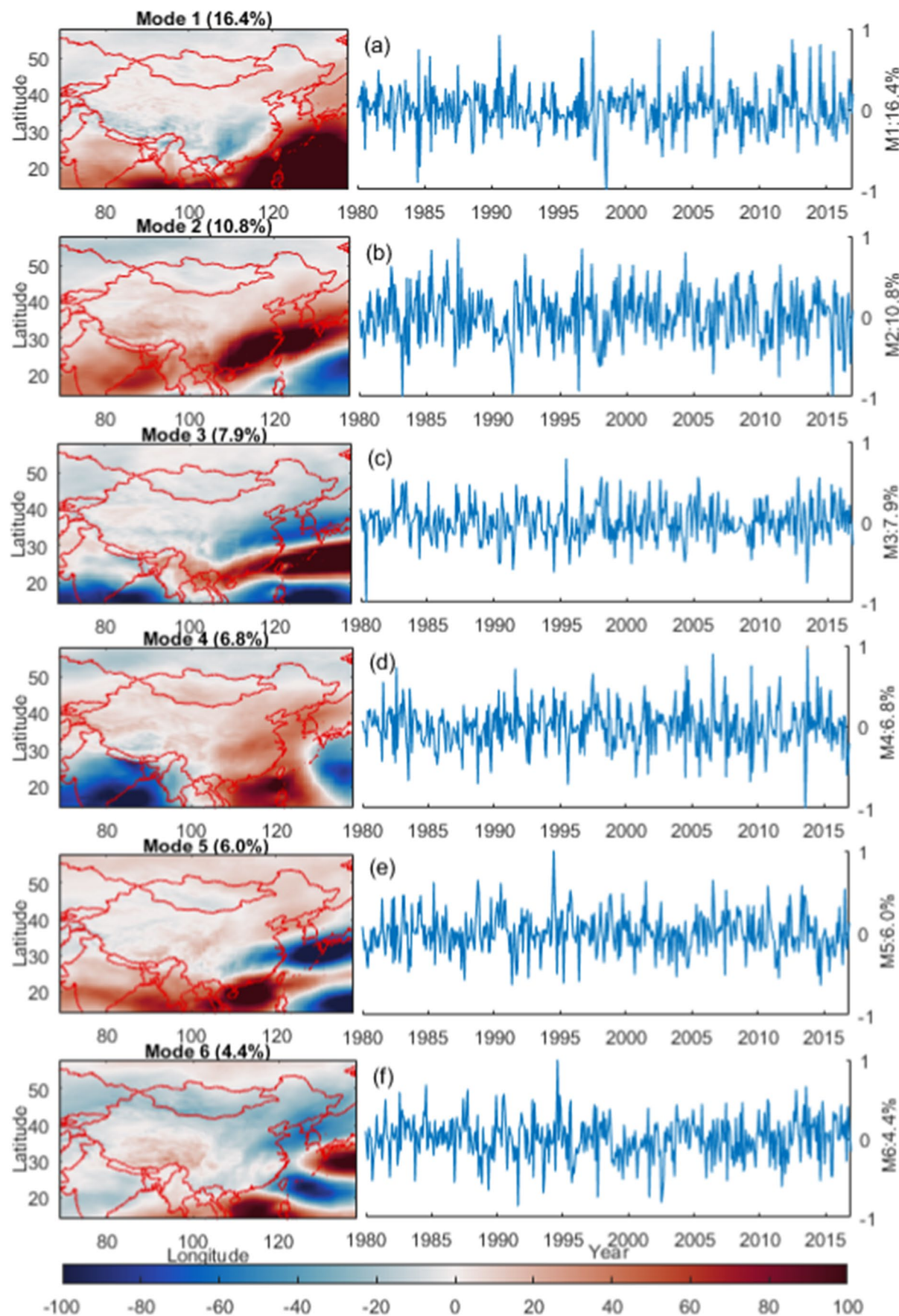
regions, respectively. This is because of the dry, cold air, and the shorter atmospheric column at the high elevations of the Tibetan Plateau, and because Mongolia is at higher latitudes affected by the perennial cold of the Siberian High (Xie et al., 2014; Guan et al., 2019).

Figure 9b shows the temporal variability of ENSO indices from 1980 to 2016. Whenever the threshold ($\pm 0.50^{\circ}\text{C}$) of the ENSO indices is satisfied during at least five continuous overlapping periods, the cold and warm events are determined accordingly (cited: http://www.cpc.ncep.noaa.gov/products/analysis_monitoring/ensostuff/ensoyears.shtml). ENSO events are separated at ± 1.0 and ± 2.0 degrees to classify El Niño and La Niña periods, respectively. The red and blue lines represented moderate and strong El Niño and La Niña phenomena, respectively. Through 1980 and 2016, we recorded 3, 3, 2, and 3 strong El Niño events and 5 moderate La Niña events for Nino-3, Nino-3.4, Nino-4, and Mei.v2, respectively. All the strongest El Niño events recorded were all in accordance with those on record during 1982–1983, 1997–1998, and 2014–2016 (Hao et al., 2019; Huang et al., 2019), which could impact IVT variability.

3.4.2 Impacts of ENSO on moisture transport variability

The CWT is a time–frequency localization analysis method used in our study to analyse localized intermittent oscillations in the IVT and ENSO time-series. It expands the one-dimensional signals in the time and frequency domains and clearly explains many kinds of change cycles hidden in the time-series (Grinsted et al., 2004; Guan et al., 2019). The wavelet analysis between ENSO indices and IVT in different climatic regions of China are shown in Fig. 10, and the result highlights some predominant scales of variability and time period (i.e., view Fig. 10 caption for wavelet explanation).

In each region, the IVT-Nino3, IVT-Nino3.4, IVT-Nino4, and IVT-MEI.v2 were qualitatively similar; however, coherence was increasing in Regions 3, 6, 7, and EMC. The cross-wavelet coherence investigation explicated that IVT and ENSO were coherent, possessing a duration of about 2–8 years, illustrated by the yellow spots in this time scale (Kao and Yu 2009). In particular, variations in the number, strength, and duration of ENSO events affecting IVT occurred every 2–4 years in Region 3, but every 2–8 years in Regions 6 and 7. Beyond 8 years, the coherence showed lower frequencies. As ENSO impacts the WPSH, it becomes strong and intrudes the west, which transports moisture from the east (Chen et al., 2014; Zhang, 2020), increasing south China precipitation. This study thus suggests that enhanced El Niño activity in the equatorial easterly pacific has a link with enhanced IVT, particularly in Sub-regions 3, 6, 7, and EMC.



◀Fig. 6 EOF spatial patterns of the first six IVT modes (*left panel*) as well as the time series of the principal components (PCs) associated with the first six EOF modes (**a–f**; *right panel*), calculated from 1980 to 2016 period over China and surrounding regions. M1–M6 indicate the percentages explained by the first six modes

3.5 Implications of ENSO variability

El Niño's relationship with its climatic counterpart, the Southern Oscillation, has been widely reported in many parts of the world (Philander 1986; Kim et al., 2017; Yu et al., 2019). El Niño event intensities vary yearly and are capable of altering atmospheric flow, influencing normal weather conditions (Chang et al. 2016; Huang et al. 2019). Generally, ENSO influences the East Asian microclimate, resulting in anticyclonic anomalies across the Philippine Sea and irregular south-westerly breezes on its northern side throughout the mature and decay stages of El Niño (Chen et al., 2014; Kao and Yu 2009; Wang et al. 2000; Ghodichore et al. 2017). The IVT difference between El Niño and La Niña years confirms that the anticyclonic anomaly of IVT is enhanced during El Niño years, indicating southwesterly IVT from the South China Sea, which increases southern China precipitation (Kim et al., 2017; Yu et al., 2019). This could possibly explain reasons for high IVT over Regions 3, 6, 7, and EMC.

The extreme summer precipitation in 1998 caused by the super 1997–1998 El Niño forced the precipitation to deviate from normal. This showed that ENSO atmospheric circulations could contribute to unusual precipitation by forcing IVT (Lau and Weng, 2001; Zhang, 2020). Along with precipitation and IVT, ENSO events have a strong impact on drought variations in China, with a signal ranging from 16 to 64 months, which is consistent with ENSO periodicity of 2–7 years (Huang et al., 2019). Since ENSO events are usually prior to drought onset, they can be used as an input factor of an early drought warning system to enhance drought prediction accuracy (Huang et al., 2019). Other studies on the impact of El Niño events (Chang et al., 2016; Yu et al., 2019) or the average intensity of an El Niño event have been studied.

Finally, Wu et al. (2012) disclosed the probable impact of shifts in the mean phase, position, and extent of SST irregularities within the southern Indian Ocean. Distinctly, the mean phase change might move the position of the mean WPSH, which successively dislodges the position of the abnormal rain area (Ghodichore et al. 2017). It seems that the abnormal SST is the principal driver for ENS, which actually modulates IVT variability patterns.

4 Summary and conclusion

This paper studied integrated moisture transport variability, with regards to their patterns, impacts and relationship with El Niño–Southern Oscillation (ENSO) across climatic regions of China from 1980 to 2016 using CFSR daily reanalysis datasets and EOF analysis procedures. We estimated the mean, interannual, and seasonal moisture transport to understand their patterns as well as investigate their importance to regional atmospheric water budgets. Furthermore, we examined typical drought and flood episodes in southern China to illustrate the role of variation in moisture transport. Finally, we examined the relationship between IVT and ENSO indices using wavelet analysis to show how ENSO could autonomously affect IVT in various climatic regions. The key outcomes are summed as follows:

- (1) The observed IVT means and variances over the Bay of Bengal, Southern, and Eastern China Sea, and South-eastern China showed that there were high mean and variances in June, July, August, and September, which can vary significantly yearly. However, in Northern China, these values were considerably low, meaning that the monthly IVT will be more predictable from climatology.
- (2) The spatial distribution of IVT anomalies was found to be different from season to season. Summer, in particular, showed significantly higher IVT values especially over the Equatorial Western Pacific, and there was also moisture transports from the Tropical Indian Ocean to the Northwestern and Southeastern China. The divergent winds flow from Southern China to the Equatorial Western Pacific, where they converge with those from Equatorial Central Pacific.
- (3) In South-east China, there was an enhanced moisture convergence of nearly 400 kg/m/s, thus augmenting the above-average precipitation and resulting in floods in June 1998. This anomalous anticyclonic moisture circulation weakened water vapor convergence to about 250 kg/m/s, causing an insufficiency in moisture supply and hence contributing to the below-average precipitation in March 2011. Thus, it can be assumed increased (reduced) moisture within the atmosphere may influence flood (drought) in the regions nearby.
- (4) The first six modes of the EOFs together explained about 52.3%, which accounts for more than half of variation in the detrended and deseasoned IVT anomalies. The leading mode was associated with ENSO and it explained about 16.4% variance within the southern China sea and central equatorial Pacific, while the second mode revealed about 10.8% of the variance and its

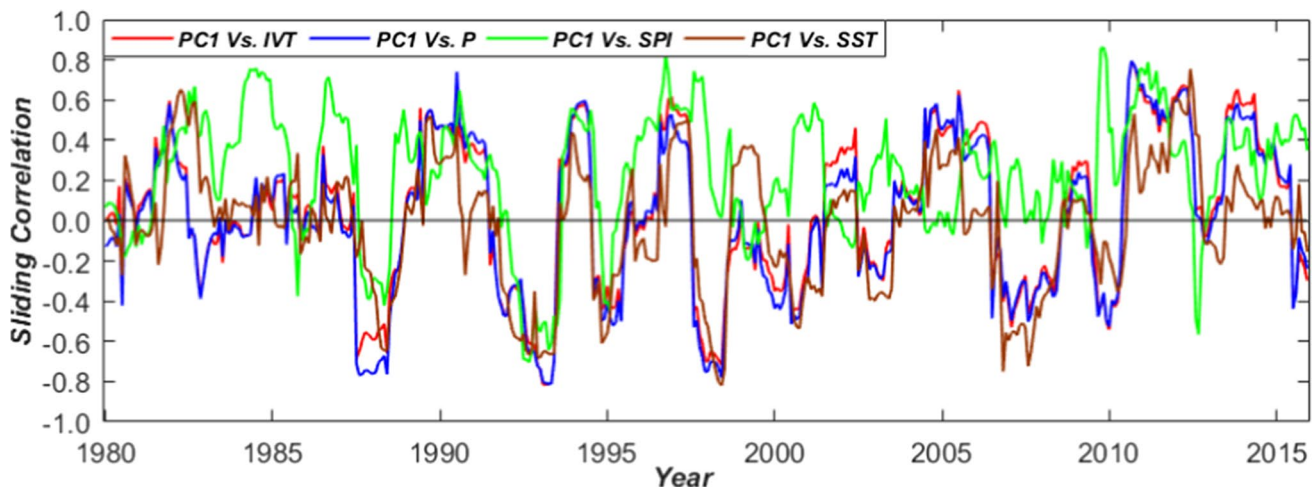


Fig. 7 Sliding correlation plots between the time series of PC1 and mean monthly de-seasoned IVT, precipitation (P), SPI index, and mean sea surface temperature (SST) between 1980 and 2016 over China

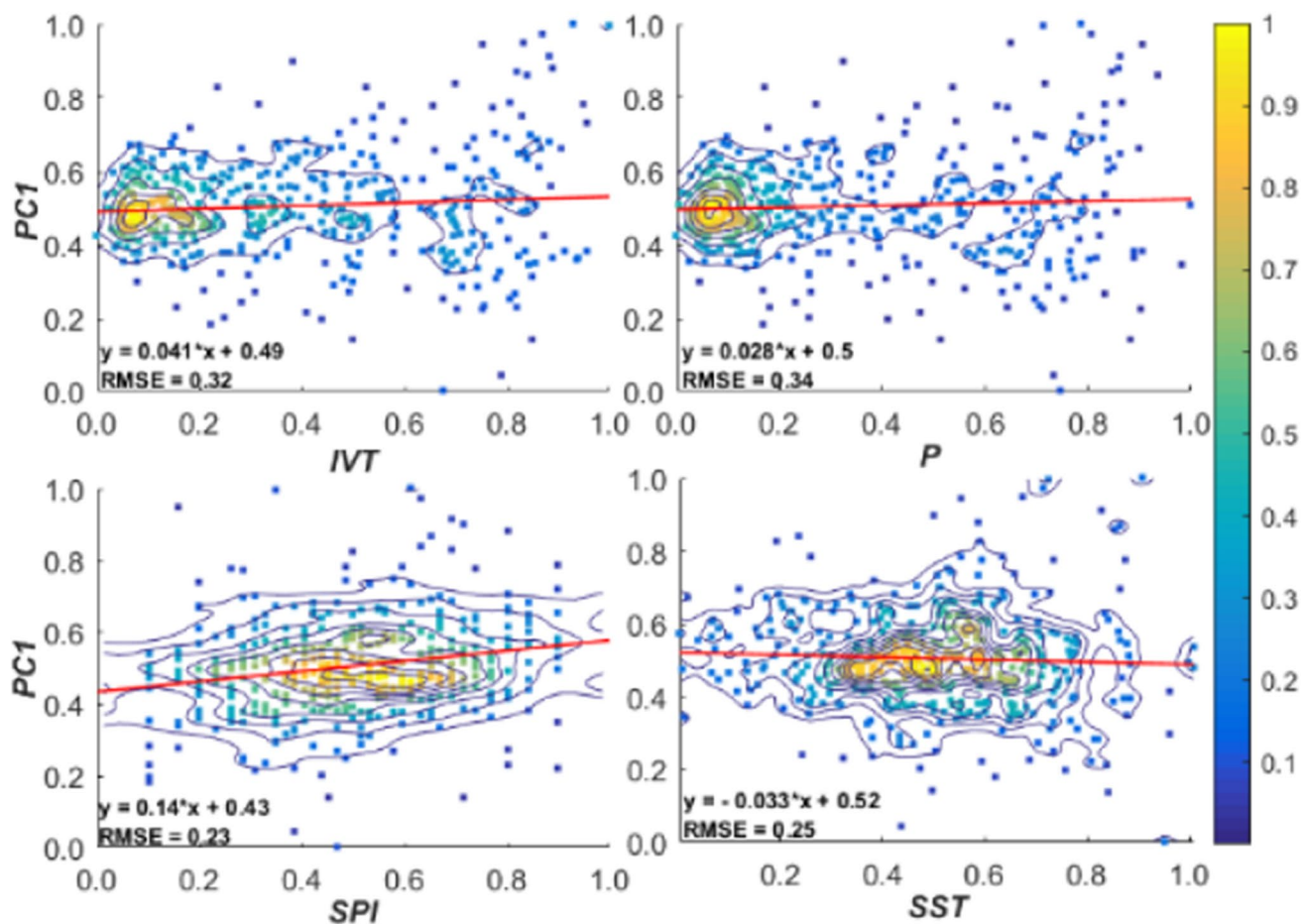


Fig. 8 Scatter plot between the time series of PC1 and standardized mean values of IVT, P , SPI index, and SST from 1980 to 2016 over China. Note: The association densities are contoured and color coded

with joint density levels of blue representing lower densities and yellow denoting higher densities. The best-fit line (solid red line) and the corresponding equation and RMSE are also shown

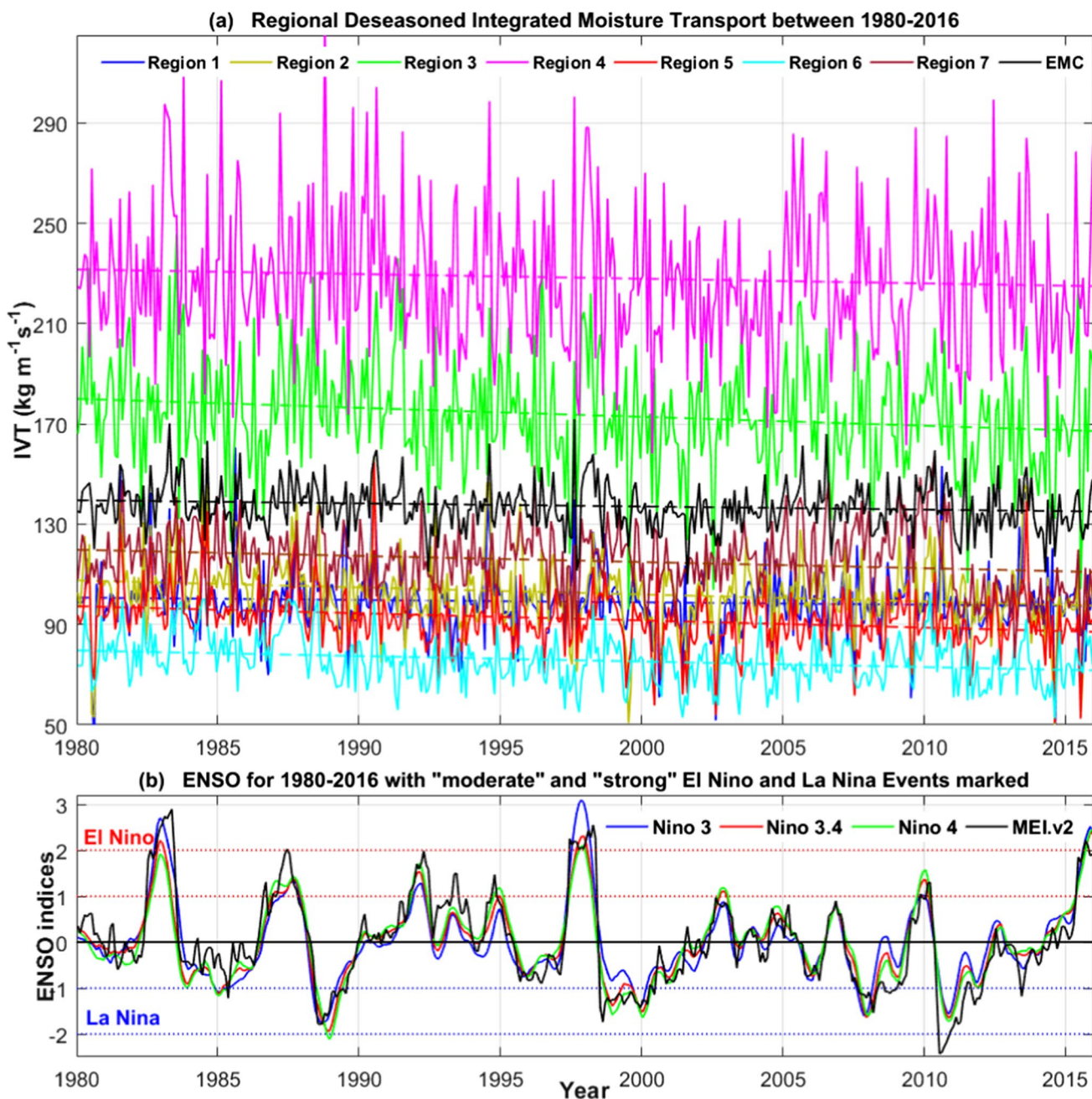


Fig. 9 **a** Temporal variations and linear trends of regionally averaged IVT ($\text{kg}/\text{m}^2/\text{s}$) within China climatic regions (Regions 1–7) and entire China (EMC) and **b** temporal variations of Nino 3, Nino 3.4, Nino 4, and MEI.v2 indices between 1980 and 2016. Note: Nino 3, Nino 3.4,

and Nino 4 are derived from SST while MEI.v2 was derived from SLP, zonal and meridional wind, SST, air temperature, and cloudiness fraction. The red and blue lines represent moderate and strong El Nino and La Nina events, respectively

- strongest in the east China sea, reaching across south-eastern China.
- (5) The sliding correlations between PC1-IVT, PC1-precipitation, PC1-SPI, and PC1-SST within a window of 12-month all fluctuated between –0.8 and 0.8. We discovered that drought measured with SPI seems to be related more to IVT than precipitation and global SST.

- (6) The cross-wavelet coherence recorded that the IVT and ENSO time series are coherent with 2–8 years period, and unusually growing in Regions 3, 6, 7, and entire EMC. This does propose that elevated IVT was associated with enhanced ENSO activities.

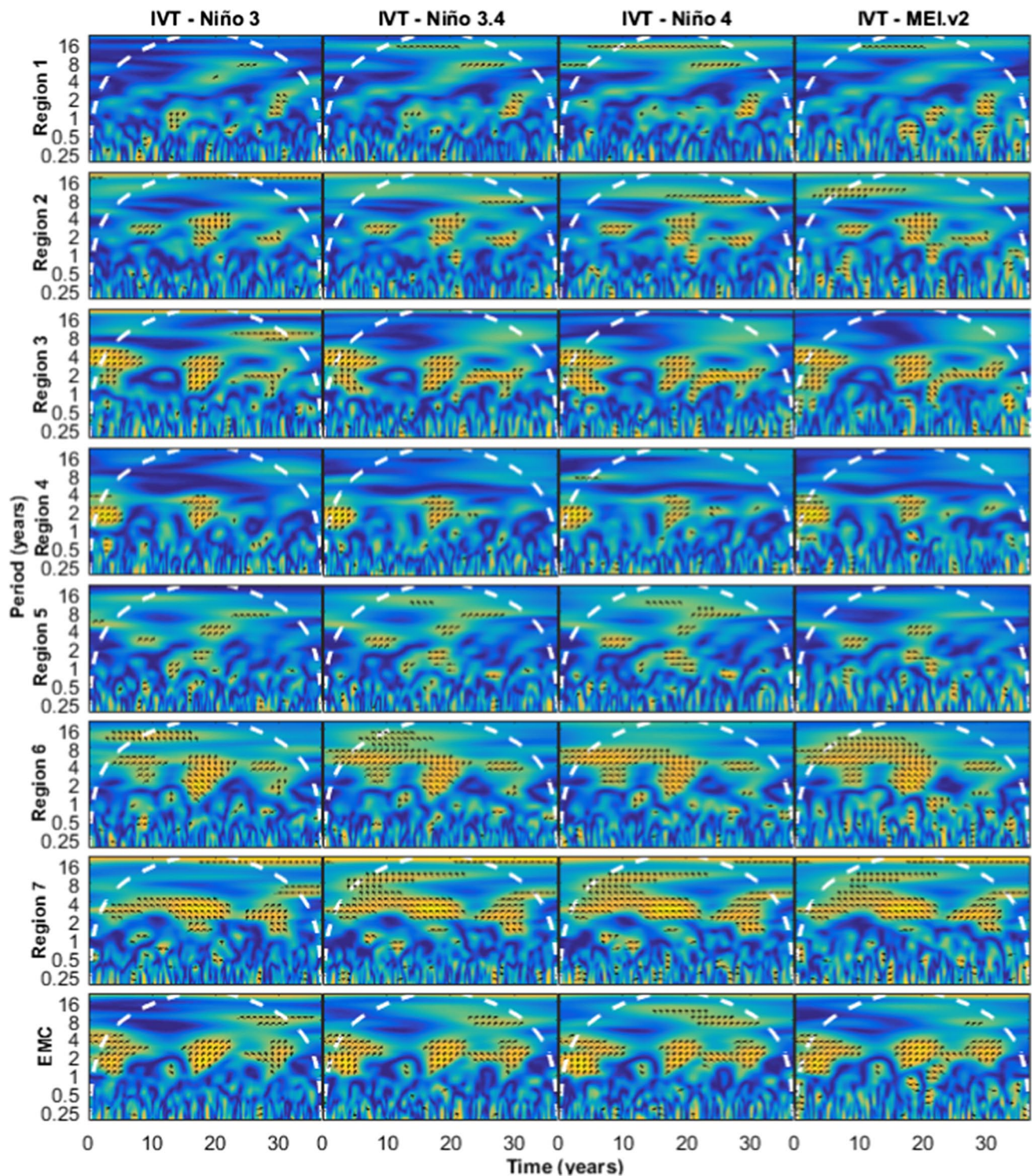


Fig. 10 Cross wavelet spectrum analysis between IVT timeseries (*cf.* Figure 9a) and ENSO indices (*cf.* Figure 9b) in different climatic regions and entire China between 1980 and 2016. Note: Column 1 (IVT and Nino 3), column 2 (IVT and Nino 3.4), column 3 (IVT and Nino 4), column 4 (IVT and MEI.v2). The thick black contours

depict the 5% confidence level of local power relative to red noise, and the black line is the cone of influence. Right-pointing arrows indicate that the two signals are in phase while left-pointing arrows are for antiphase signals

While we have conducted statistical investigations to establish the influence of ENSO on moisture transport, further studies will be required in the future to substantiate our results and to explore the association between IVT and other climate indices. In addition to this, one of the newly emerged approaches is Atmospheric Rivers (ARs) identification, which is often referred to as narrow, elongated moisture streams that are capable of propelling hydrological extremes such as heavy precipitation during landfall (Waliser and Guan 2017). Lately, many researchers have considered the connections between ARs and hydrological severe events (Guan and Waliser 2015; Lavers and Villarini 2015). Consequently, in line with Ghodichore et al. (2017), more analysis would also be imperative for appraising ARs' roles in flood and drought events and employing the knowledge to predict likely events. This study could contribute to a better perception of how atmospheric circulation may change the overall flow of the atmosphere to have an effect on traditional climatic conditions in China.

Author contribution All authors contributed to the study. Olusola O. Ayantobo: conceptualization, investigation, methodology, software, formal analysis, writing—original draft, writing—review and editing. Jiahua Wei: conceptualization, investigation, methodology, writing—review and editing, project administration, funding acquisition. Beiming Kang: writing—review and editing. Guanqian Wang: project administration, funding acquisition, writing—review and editing. All authors read and agreed with the final manuscript.

Funding This study was jointly supported by the National Key R&D Program of China (2017YFC0403600, 2016YFE0201900), National Natural Science Foundation of China (91847302), the Research Fund Program of State Key Laboratory of Hydroscience and Engineering of Tsinghua University (2017-KY-04, 2019-KY-01), and Major Science and Technology Project of Qinghai Province (2021-SF-A6).

Availability of data and material The datasets analyzed during the current study are The Climate Forecast System Reanalysis datasets versions CFSv1 and CFSv2 (<https://rda.ucar.edu/datasets/ds093.1/> and <https://rda.ucar.edu/datasets/ds094.1/>) from the National Centers for Environmental Prediction (NCEP), and the teleconnection indices datasets from the National Oceanic and Atmospheric Administration's Earth Systems Research Laboratory accessible at <http://www.esrl.noaa.gov/psd/data/gridded/>. The data generated in this study are available from the corresponding author upon reasonable request.

Code availability The code used in this research may be available on request to the corresponding author.

Declarations

Ethics approval and consent to participate The authors declare that there is no human or animal participant in the study. All the authors consent to participate in the research.

Consent for publication The authors give their consent to the publication of all details of this manuscript including texts, figures, and tables in the journal of Theoretical and Applied Climatology.

Conflict of interest The authors declare no competing interests.

References

- Abramowitz M, Stegun IA (1965) Handbook of mathematical functions. Dover Publications, New York
- Ayantobo OO, Li Y, Song S (2019) Multivariate drought frequency analysis using four-variate symmetric and asymmetric Archimedean copula functions. *Water Resour Manage* 33:103–127
- Ayantobo OO, Li Y, Song S, Yao N (2017) Spatial comparability of drought characteristics and related return periods in mainland China over 1961–2013. *J Hydrol* 550:549–567
- Chang L, Xu J, Tie X et al (2016) Impact of the 2015 El Niño event on winter air quality in China. *Sci Rep* 6:34275
- Chen H, Xu CY, Guo S (2012) Comparison and evaluation of multiple GCMs, statistical downscaling, and hydrological models in the study of climate change impacts on runoff. *J Hydrol* 434:36–45
- Chen J, Wen Z, Wu R, Chen Z, Zhao P (2014) Interdecadal changes in the relationship between Southern China winter-spring precipitation and ENSO. *Clim Dyn* 43:1327–1338
- Dong W et al (2016) Summer rainfall over the southwestern Tibetan Plateau controlled by deep convection over the Indian subcontinent. *Nat Commun* 7:10925
- Dufour A, Zolina O, Gulev SK (2016) Atmospheric moisture transport to the arctic: assessment of reanalyses and analysis of transport components. *J Clim* 29(14):5061–5081
- Feng L, Zhou T (2012) Water vapor transport for summer precipitation over the Tibetan Plateau: multidata set analysis. *J Geophys Res Atmos* 117:D20114
- Fu S, Li D, Sun J, Si D, Ling J, Tian F (2016) A 31-year trend of the hourly precipitation over South China and the associated mechanisms. *Atmos Sci Lett* 17:216–222
- Ghodichore N, Dhanya CT, Vinnarasi R (2017) Examination of mean precipitation and moisture transport in reanalysis products over India. *ISH Journal of Hydraulic Engineering*. <https://doi.org/10.1080/09715010.2017.1364983>
- Gimeno, L., Nieto, R., Vázquez, M., Lavers, D. A. 2014. Atmospheric rivers: a mini-review, *Front. Earth Sci.*, 2, 2.1–2.6.
- Gong, D.Y., Ho, C.H. 2002. Shift in the summer rainfall over the Yangtze River valley in the late 1970s. *Geophys. Res. Lett.*, 29(10).
- Grinsted A, Moore JC, Jevrejeva S (2004) Application of the cross wavelet transform and wavelet coherence to geophysical time series. *Nonlinear Process Geophys* 11:561–566
- Guan B, Waliser DE (2015) Detection of atmospheric rivers: evaluation and application of an algorithm for global studies. *J Geophys Res Atmos* 120(24):12514–12535
- Guan XF, Yang LM, Zhang YX, Li JG (2019) Spatial distribution, temporal variation, and transport characteristics of atmospheric water vapor over Central Asia and the arid region of China. *Global Planet Change* 172:159–178
- Hao ZC, Hao FH, Singh VP, Zhang X (2019) Statistical prediction of the severity of compound dry-hot events based on El Niño–Southern Oscillation. *J Hydrol* 572:243–250
- Herrera-Estrada JE, Martinez JA, Dominguez F, Findell KL, Wood EF, Sheffield J (2019) Reduced moisture transport linked to drought propagation across North America. *Geophys Res Lett* 46:5243–5253
- Huang SZ, Wang L, Wang H, Huang Q, Leng GY, Fang W, Zhang Y (2019) Spatio-temporal characteristics of drought structure across China using an integrated drought index. *Agr Water Manage* 218:182–192
- Kao HY, Yu JY (2009) Contrasting eastern-Pacific and central-Pacific types of ENSO. *J Clim* 22:615–632

- Kim JW, An SI, Jun SY et al (2017) ENSO and East Asian winter monsoon relationship modulation associated with the anomalous north-west Pacific anticyclone. *Clim Dyn* 49(4):1157–1179
- Lamjiri M, Dettinger M, Ralph F, Guan B (2017) Hourly storm characteristics along the U.S. west coast: role of atmospheric rivers in extreme precipitation. *Geophys Res Lett* 44:7020–7028
- Lau K, Weng H (2001) Coherent modes of global SST and summer rainfall over China: an assessment of the regional impacts of the 1997–98 El Niño. *J Clim* 14:1294–1308
- Lavers DA, Villarini G (2015) The contribution of atmospheric rivers to precipitation in Europe and the United States. *J Hydrol* 522:382–390
- Lélé MI, Leslie LM, Lamb PJ (2015) Analysis of low-level atmospheric moisture transport associated with the West African monsoon. *J Clim* 28(11):4414–4430
- Li H, Zhang W, He J et al (2016) Influences of annual SST cycle on local air-sea processes during El Niño events. *Acta Oceanol Sin* 38(1):56–68
- Li HQ, Wan QL, Peng DD, Liu XT, Xiao H (2020) Multiscale analysis of a record-breaking heavy rainfall event in Guangdong. *China Atmos Res* 232:104–703
- Li, Y., Lin, Z. 2018. Three-dimensional structure of atmospheric water vapor transportation and its relationship with the summer flood/drought situations over Huaihe River Basin, 2018, IOP Conference Series: Earth and Environmental Science
- Li, X., Wen, Z., Zhou, W., Wang, D. 2012. Atmospheric water vapor transport associated with two decadal rainfall shifts over East China, Journal of the Meteorological Society of Japan. Ser. II, <https://doi.org/10.2151/jmsj.2012-501>
- Li Z, Chen J, Dong X (2014) Comparison analysis for summer heavy drought and its circulation features in 2011/2006 in Chongqing (in Chinese). *J Southwest Univ Nat Sci Edit* 36(8):1–10
- Liu R, Sun J, Wei J, Fu S (2016) Classification of persistent heavy rainfall events over South China and associated moisture source analysis. *J Meteorol Res* 30:678–693
- Liu Z, Lu G, He H, Wu Z, He J (2017) Anomalous features of water vapor transport during severe summer and early fall droughts in southwest China. *Water* 9:244
- Ma YZ, Lu MQ, Chen HN, Pan MX, Hongbe Y (2018) Atmospheric moisture transport versus precipitation across the Tibetan Plateau: a mini-review and current challenges. *Atmos Res* 209:50–58
- Marengo J, Gimeno L, Dominguez F, Nieto R, Trigo R, Drumond A, Reason CJC, Kumar R (2016) Major mechanisms of atmospheric moisture transport and their role in extreme precipitation events major mechanisms of atmospheric moisture transport and their role in extreme precipitation events. *Annu Rev Environ Res* 41:117–141
- Maussion F, Scherer D, Mölg T, Collier E, Curio J, Finkelnburg R (2014) Precipitation seasonality and variability over the Tibetan Plateau as resolved by the high Asia reanalysis. *J Clim* 27:1910–1927
- McKee, T.B., Doesken, N.J., Kleist, J. 1995. Drought monitoring with multiple time scales. In: Proceedings of the 9th Conference on Applied Climatology. American Meteorological Society, Dallas, Tex, USA, pp. 233–236.
- McPhaden MJ, Zebiak SE, Glantz MH (2006) ENSO as an integrating concept in earth science. *Science* 314:1740
- Messie M, Chavez F (2011) Global modes of sea surface temperature variability in relation to regional climate indices. *J Clim* 24:4314–4331
- Peixóto, J.P. 1973. Atmospheric vapor flux computations for hydrological purposes. WMO Publ
- Philander SGH (1986) Unusual conditions in the tropical Atlantic Ocean in 1984. *Nature* 322:236–238
- Qian W, Qin A (2008) Precipitation division and climate shift in China from 1960 to 2000. *Theor Appl Climatol* 93(1–2):1–17
- Roy T, Martinez JA, Herrera-Estrada JE, Zhang Y, Dominguez F, Berg A, Ek M, Wood E (2019) Role of moisture transport and recycling in characterizing droughts: perspectives from two recent US droughts and the CFSv2 system. *J Hydrometeorol* 20:139–154
- Ruizbarradas A, Nigam S (2013) Atmosphere–land surface interactions over the southern great plains: characterization from pentad analysis of DOE ARM field observations and NARR. *J Clim* 26(3):875–886
- Saha S, Moorthi S, Pan HL, Wu X, Wang J, Nadiga S, Tripp P, Kistler R, Woollen J, Behringer D, Liu H, Stokes D, Grumbine R, Gayno G, Wang J, Hou YT, Chuang HY, Juang HMH, Sela J, Iredell M, Treadon R, Kleist D, Van Delst P, Keyser D, Derber J, Ek M, Meng J, Wei H, Yang R, Lord S, Van Den Dool H, Kumar A, Wang W, Long C, Chelliah M, Xue Y, Huang B, Schemm JK, Ebisuzaki W, Lin R, Xie P, Chen M, Zhou S, Higgins W, Zou CZ, Liu Q, Chen Y, Han Y, Cucurull L, Reynolds RW, Rutledge G, Goldberg M (2010) The NCEP climate forecast system reanalysis. *Bull Am Meteorol Soc* 91(8):1015–1057
- Simmonds I, Bi DH, Hope P (1999) Atmospheric water vapor flux and its association with rainfall over China in summer. *J Clim* 12:1353–1367
- Smith TM, Reynolds RW, Peterson TC, Lawrimore J (2008) Improvements to NOAA's historical merged land-ocean surface temperature analysis (1880–2006). *J Clim* 21:2283–2296
- Sun C, Yang S (2012) Persistent severe drought in southern China during winter–spring 2011: large-scale circulation patterns and possible impacting factors. *J Geophys Res* 117:D10112
- Torrence C, Compo GP (1998) A practical guide to wavelet analysis. *B Am Meteorol Soc* 79:61–78
- Waliser D, Guan B (2017) Extreme winds and precipitation during landfall of atmospheric rivers. *Nature Geosci* 10(3):179–183
- Wang B, Wu R, Fu XH (2000) Pacific–East Asia teleconnection: how does ENSO affect East Asian climate? *J Clim* 13:1517–1536
- Wang L, Chen W, Zhou W, Huang G (2015) Drought in Southwest China: a review. *Atmos Oceanic Sci Lett* 8:339–344
- Wang L, Chen W, Zhou W, Huang G (2016) Understanding and detecting super-extreme droughts in Southwest China through an integrated approach and index. *Q J R Meteorol Soc* 142(694):529–535
- Wu R, Wang B (2000) Interannual variability of summer monsoon onset over the western North Pacific and the underlying processes. *J Clim* 13:2483–2501
- Wu R, Yang S, Wen Z, Huang G, Hu K (2012) Interdecadal change in the relationship of southern China summer rainfall with tropical Indo-Pacific SST. *Theor Appl Climatol* 108:119–133
- Wu ZY, Lu GH, Wen L, Lin CA (2011) Reconstructing and analysing China's fifty-nine-year (1951–2009) drought history using hydrological model simulation. *Hydrol Earth Syst Sci Discuss* 8(1):1861–1893
- Xie CY, Li MJ, Zhang XQ (2014) Characteristics of summer atmospheric water resources and its causes over the Tibetan plateau in recent 30 years. *J Nat Resour* 29(6):979–989
- Yu XC, Wang ZL, Zhang H, Zhao SY (2019) Impacts of different types and intensities of El Niño events on winter aerosols over China. *Sci Total Environ* 655:766–780
- Yuan GH, Zhang L, Liu YB (2021) Impacts of soil moisture and atmospheric moisture transport on the precipitation in two typical regions of China. *Atmos Res* 247:105–151
- Zhang C (2020) Moisture sources for precipitation in Southwest China in summer and the changes during the extreme droughts of 2006 and 2011. *J Hydro* 591:125–333
- Zhao, S. 1983. A new scheme for comprehensive physical regionalization in China. *Acta Geographica Sinica*, 1–10 (In Chinese).
- Zhu Y, Newell R (1998) A proposed algorithm for moisture fluxes from atmospheric rivers. *Mon Wea Rev* 126:725–735

Publisher's note Springer Nature remains neutral with regard to jurisdictional claims in published maps and institutional affiliations.